# A Two-Qubit Molecular Architecture for Electron-mediated Nuclear Quantum Simulation

Matteo Atzori,[a,*] Alessandro Chiesa,[b,c] Elena Morra,[d] Mario Chiesa,[d] Lorenzo Sorace,[a] Stefano Carretta,[b,*] and Roberta Sessoli[a,*]

[a] Dipartimento di Chimica "Ugo Schiff" & INSTM, Università degli Studi di Firenze, I-50019 Sesto Fiorentino, Italy.

[b] Dipartimento di Scienze Matematiche, Fisiche e Informatiche, Università di Parma, I-43124 Parma, Italy.

[c] Institute for Advanced Simulation, Forschungszentrum Jülich, D-52425 Jülich, Germany.

[d] Dipartimento di Chimica & NIS Centre, Università di Torino, Via P. Giuria 7, I-10125 Torino, Italy.

**Corresponding Authors:**

matteo.atzori@unifi.it

stefano.carretta@fis.unipr.it

roberta.sessoli@unifi.it

**ELECTRONIC SUPPLEMENTARY INFORMATION (ESI)**

## *HYSCORE experiments*

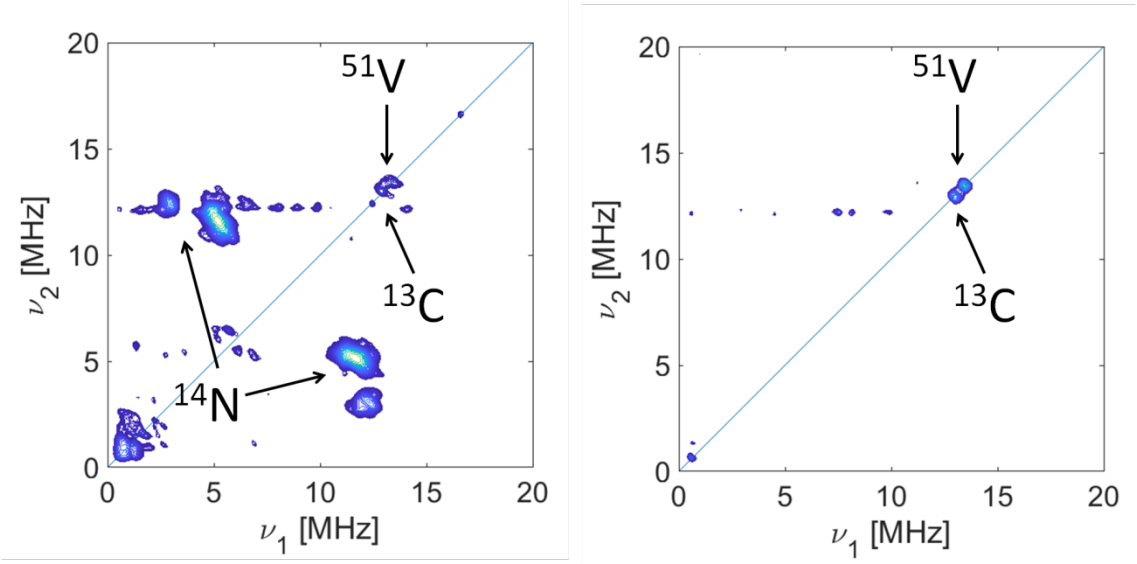


**Figure S1.** Q-band 6-pulse HYSCORE spectra of **1** in frozen solution (0.75 mM) of DMF (left) and DMSO (right), recorded at 15 K. The $^{13}$C diagonal peak, indicated in the figures, is due to the hyperfine interaction to the matrix $^{13}$C carbon nuclei. Due to the low natural abundance (1.07 %) of $^{13}$C isotopes, only remote carbon nuclei are detected, the observation of directly coupled carbon nuclei being hampered by the low signal intensity.

## *X-band Continuous Wave Electron Paramagnetic Resonance Spectroscopy*

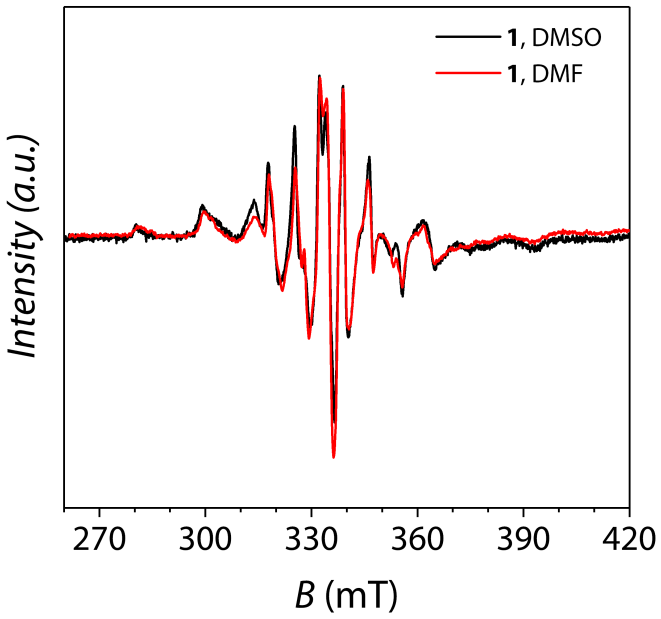


**Figure S2.** Comparison between experimental frozen solution (0.75 mM) spectra of **1** at X-band frequency (9.39 GHz) ($T$ = 10 K) in DMF (red line) and DMSO (black line).

## *Static magnetic properties*

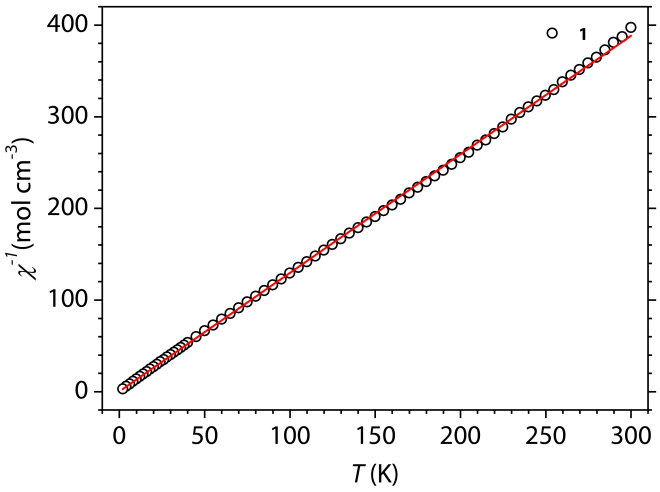


**Figure S3.** Temperature dependence of the molar magnetic susceptibility ($\chi_m^{-1}$) for **1** in the temperature range 2.0–300 K under an applied static magnetic field of 1.0 T ($T$ > 20 K) and 0.1 T ($T$ < 20 K). Solid line represents the best-fit of the data according to the Curie-Weiss law $\chi = C/T-\theta$ ($C$ = 0.77 cm$^3$ mol$^{-1}$, $\theta$ = –0.19(2) cm$^{-1}$, which are consistent with two essentially uncoupled $S$ = ½ and $g$ ~ 2.0 centers, $C$ = 0.75 cm$^3$ mol$^{-1}$).

## *Q-band Continuous Wave Electron Paramagnetic Resonance Spectroscopy*

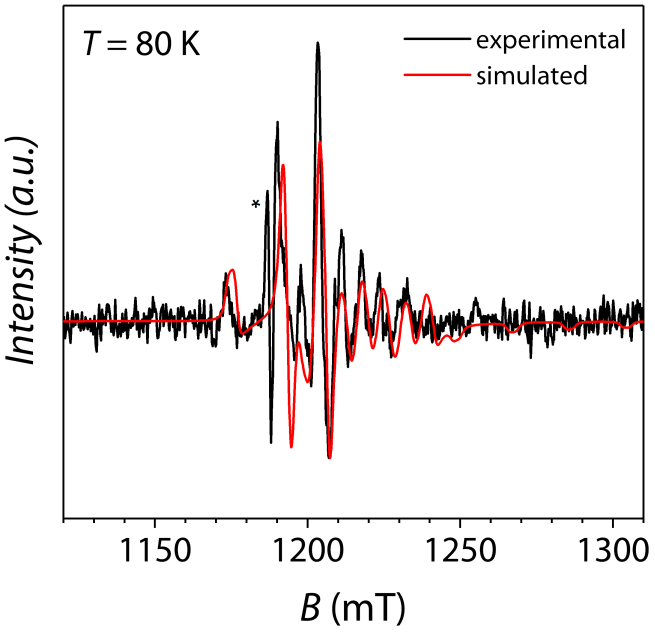


**Figure S4.** Experimental frozen solution (0.75 mM on DMF) spectrum of **1** recorded at Q-band frequency (33.7 GHz) and $T$ = 10 K (black line). Spectrum simulation (red line) obtained by using the same spin Hamiltonian parameters reproducing the X-band spectrum (Figure 3a). To account for the larger strain effects expected in Q-band with respect to X-band we assumed a H strain effect approximately four times larger at the higher frequency. Asterisk indicates the signal related to a spurious signal of the cavity.

## *Zeeman diagram*

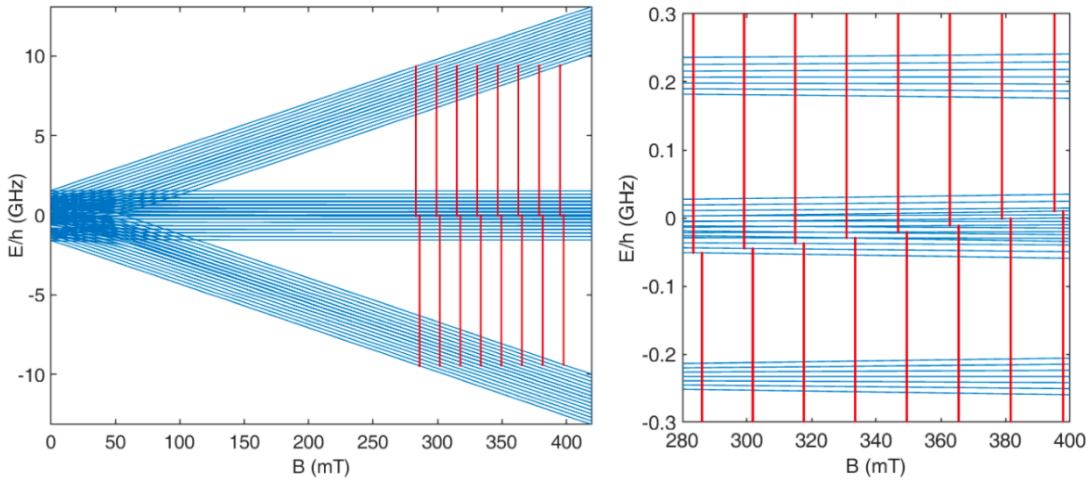


**Figure S5.** Energy diagram for **1** calculated for field applied along *z*. Red sticks represent the calculated resonance field for allowed transitions (left). Zoom of the central energy region evidencing the different states involved in the transitions (right).

## *Pulsed EPR*

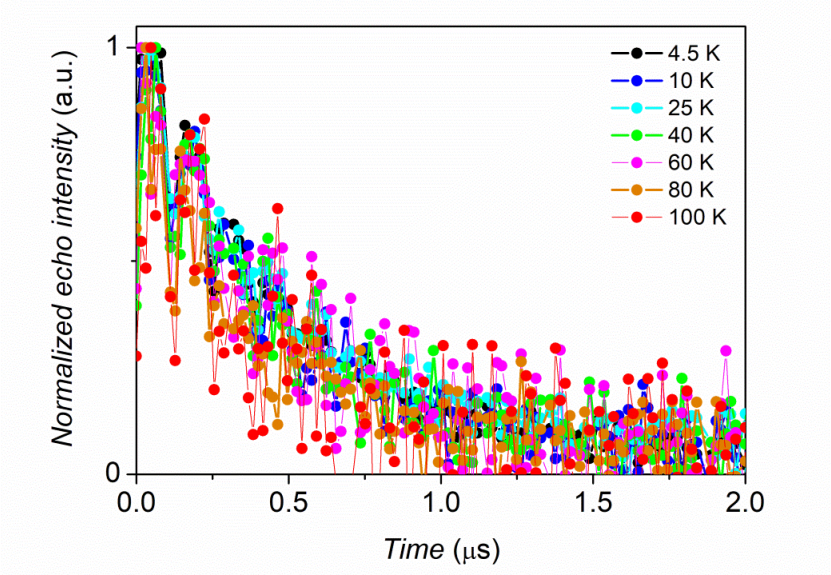


**Figure S6.** Echo decay traces recorded at X-band for **1** in frozen solution of DMSO at different temperatures.

$$T_1^{-1} = aT + bT^n$$

**Equation S1.** Equation of the model used for the fit of the temperature dependence of the spin-lattice relaxation rate ($T_1^{-1}$) obtained through pulsed-EPR spectroscopy for **1**. The first terms accounts for the direct mechanism of relaxation and the second term for a Raman mechanism of relaxation. The fit provides a value of $n$ = 2.8(1), which is typical for vanadyl-based complexes (see main text).

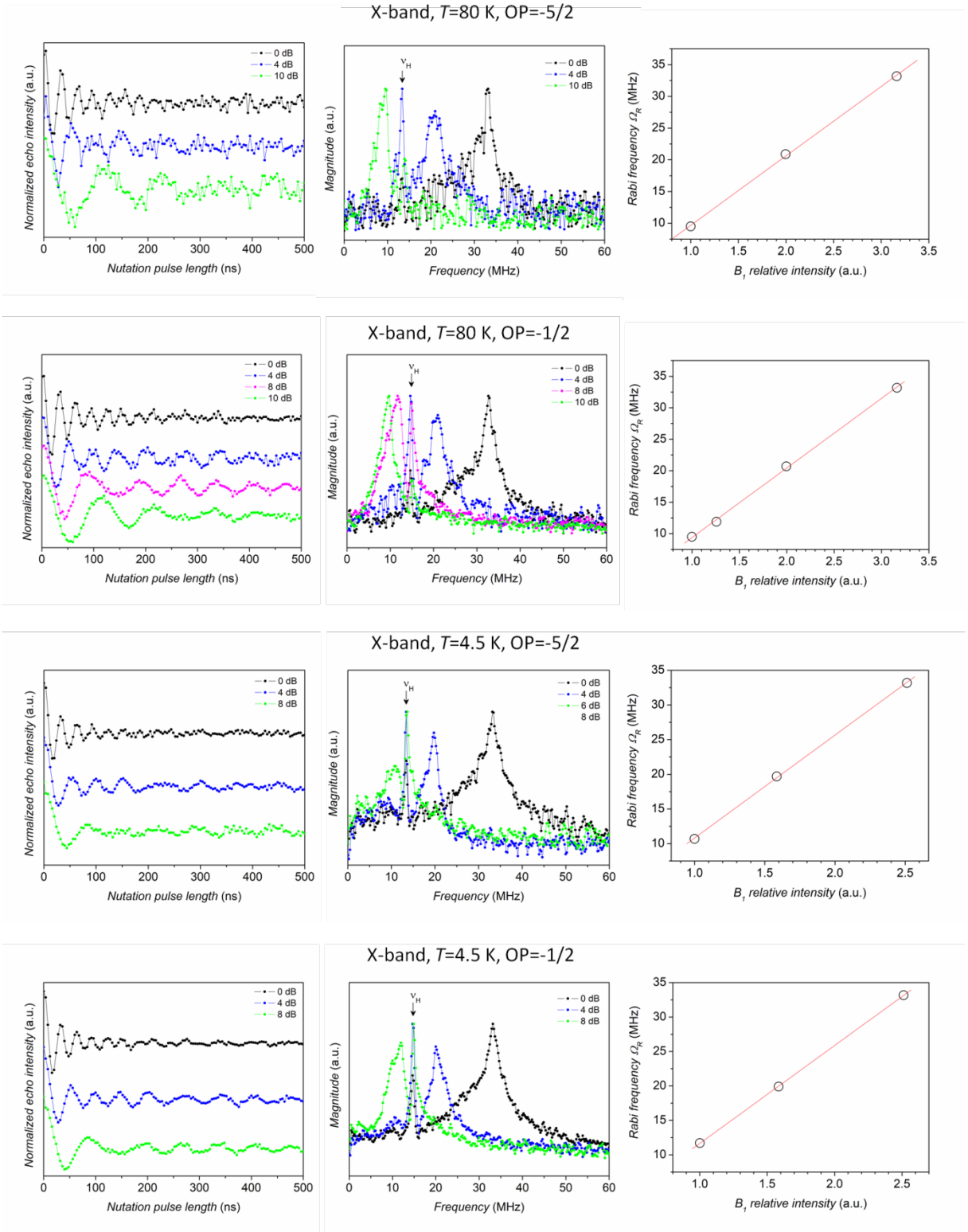


**Figure S7.** Rabi oscillations (left panels) and Fourier transform (central panels) for **1** in frozen solution of DMF recorded at X-band at 4.5 K and 80 K with different microwave attenuations. The linear dependence of the Rabi frequencies as a function of the relative intensity of the oscillating field $B_1$ is shown in the right panels.

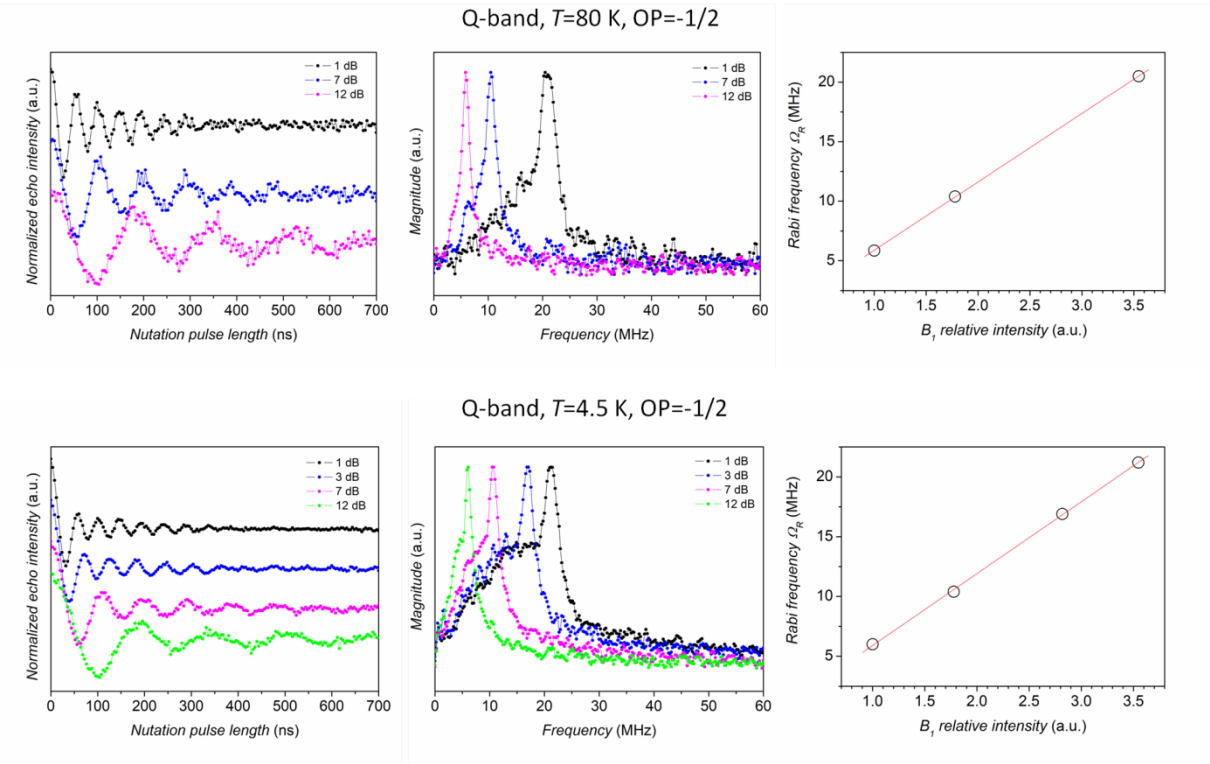


**Figure S8.** Rabi oscillations (left panels) and Fourier transform (central panels) for **1** in frozen solution of DMF recorded at Q-band at 4.5 K and 80 K with different microwave attenuations. The linear dependence of the Rabi frequencies as a function of the relative intensity of the oscillating field $B_1$ is shown in the right panels.

## *AC susceptometry*

$$\chi''(\omega) = (\chi_T - \chi_S)\frac{(\omega\tau)^{1-\alpha}\cos\left(\frac{\pi\alpha}{2}\right)}{1 + 2(\omega\tau)^{1-\alpha}\sin\left(\frac{\pi\alpha}{2}\right) + (\omega\tau)^{2-2\alpha}}$$

**Equation S2.** Equation of the Debye model used for the extrapolation of the relaxation times $\tau$ through AC susceptibility measurements. $\chi''$ is the imaginary susceptibility, $\chi_T$ is the isothermal susceptibility, $\chi_S$ is the adiabatic susceptibility, $\omega$ is the angular frequency, and $\alpha$ is the distribution width of the relaxation time.

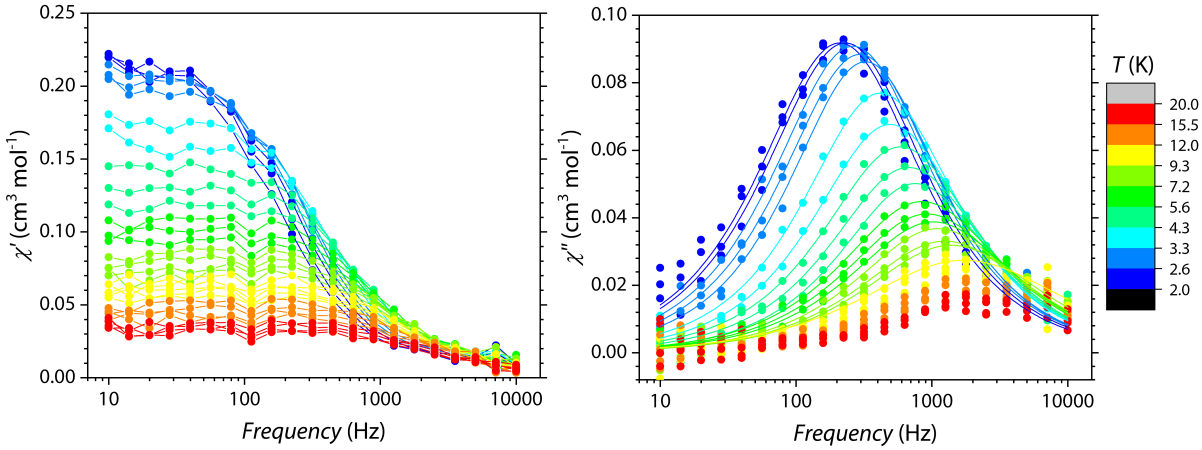


**Figure S9.** Frequency dependence of the real component $\chi'$ (left) and the imaginary component $\chi''$ (right) of the magnetic susceptibility of **1** as a function of the temperature (2.0–20 K range) under an applied static magnetic field of 1.0 T. For $\chi''$, the continuous lines represent the best-fit to the Debye equation (Eq. S1).

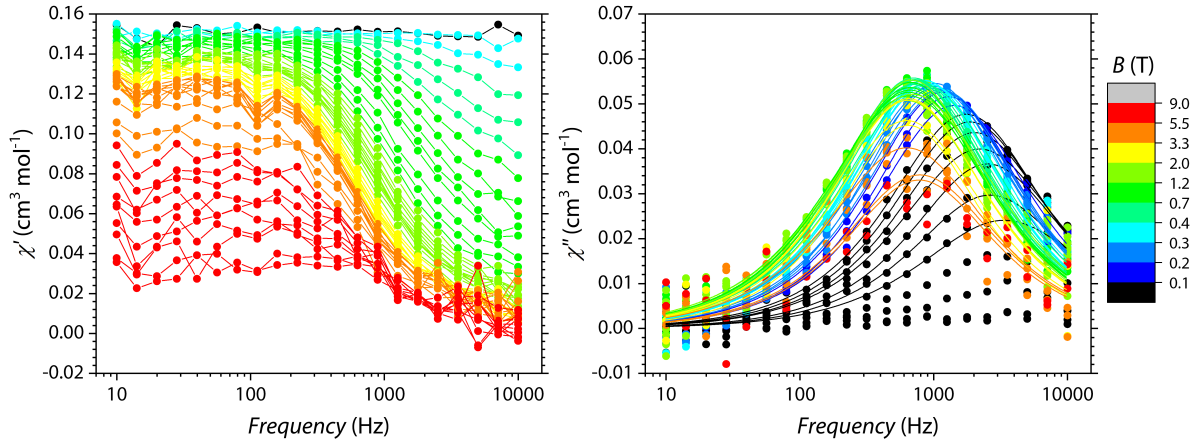


**Figure S10.** Frequency dependence of the real component $\chi'$ (left) and the imaginary component $\chi''$ (right) of the magnetic susceptibility of **1** as a function of the static magnetic field (0.00–8.5 T range) at $T$ = 5 K. For $\chi''$, the continuous lines represent the best-fit to the Debye equation (Eq. S1).

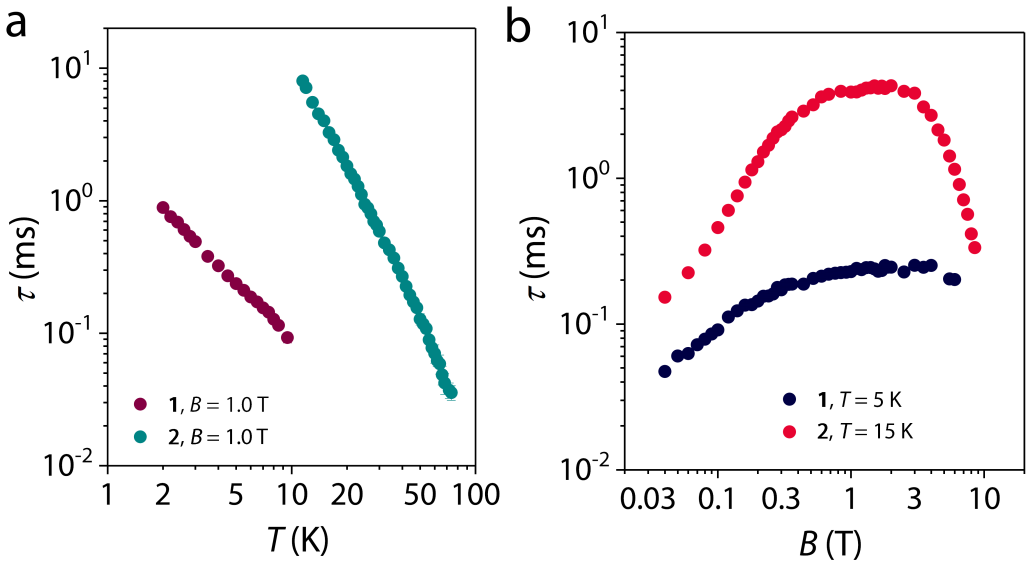


**Figure S11.** (a) Temperature and (b) field dependence of $\tau$ extracted from AC susceptibility measurements for compounds **1** and **2**.

## *Computational details*

**Dynamics of Open Quantum Systems.** The dynamics of the system subject to the pulse sequence used to implement quantum gates and quantum simulations reported in Figures 4-5 (main text) is determined by the numerical solution of the Lindblad equation:

$$\frac{d\rho}{dt} = -i[H,\rho] + \sum_i \mathcal{L}_i[\rho]$$

Here ρ is the system density matrix, $H$ the full system Hamiltonian (Eq. 1, main text) and

$$\mathcal{L}_i[\rho] = \frac{1}{T_m}\left(2s_{zi}\rho s_{zi} - \frac{\rho}{2}\right)$$

is the Lindblad superoperator, depending on spin ½ operators $s_i$ acting on the electronic spins. It accounts for the pure dephasing dynamics induced by the finite value of $T_m$. See Ref. 1 for a detailed treatment on modeling the effect of the environment on the evolution of open quantum systems. Since the nuclear $T_m$ (as well as nuclear and electronic relaxation times) is much longer than the gating time, it has been neglected in the present simulations.

**Quantum Gates.** We overview here some basic concepts about single- and two-qubit gates[2] and provide some details about their implementation with the present architecture. Single-qubit gates are independent rotations of the qubits. They can be expressed in terms of Pauli matrices, which, in the standard basis representation, read

$$\sigma_x = \begin{pmatrix} 0 & 1 \\ 1 & 0 \end{pmatrix} \quad \sigma_y = \begin{pmatrix} 0 & -i \\ i & 0 \end{pmatrix} \quad \sigma_z = \begin{pmatrix} 1 & 0 \\ 0 & -1 \end{pmatrix}.$$

In particular, a rotation about $\alpha$ axis of the Bloch sphere of an angle $\vartheta$ is given by

$$R_\alpha(\vartheta) = e^{-i\frac{\sigma_\alpha}{2}\vartheta}.$$

Hence, rotations about the *z* axis

$$R_z(\vartheta) = \begin{pmatrix} e^{-i\vartheta/2} & 0 \\ 0 & e^{i\vartheta/2} \end{pmatrix}$$

account for a relative phase shift between the two components of the single-qubit wave-function. Conversely, rotations about *x*

$$R_x(\vartheta) = \begin{pmatrix} \cos\frac{\vartheta}{2} & -i\sin\frac{\vartheta}{2} \\ -i\sin\frac{\vartheta}{2} & \cos\frac{\vartheta}{2} \end{pmatrix}$$

or *y* axis

$$R_y(\vartheta) = \begin{pmatrix} \cos\frac{\vartheta}{2} & -\sin\frac{\vartheta}{2} \\ \sin\frac{\vartheta}{2} & \cos\frac{\vartheta}{2} \end{pmatrix}$$

correspond to a population transfer (with the proper phases) between $|0\rangle$ and $|1\rangle$ components. A generic rotation about an arbitrary axis of the Bloch sphere can be obtained by combining rotations about two non-parallel axes. We implement single-qubit rotations about *x* or *y* axis by means of radio-frequency, uniform (transverse, e.g. along x) Gaussian pulses, described by the time-dependent Hamiltonian term

$$H_1(t) = \mu_B B_1 g_x (s_{1x} + s_{2x}) e^{-\frac{(t-t_0)^2}{2\sigma^2}} \cos(\omega t + \phi),$$

in which the frequency $\omega/2\pi$ corresponds to the $|0\rangle - |1\rangle$ gap, while $\phi$ selects the rotation axis in the *x*-*y* plane and the pulse-duration $\sigma$ determines the rotation angle $\vartheta$. The pulse amplitude $B_1$ must be sufficiently small to ensure spectral resolution of the desired transition.

It is worth noting that the computational basis states are defined into the subspace in which the electron spins are frozen into the ↓↓ state and the electron and nuclear spin wavefunctions are practically factorized. However, the small mixing between electronic and nuclear states leads to a remarkable enhancement of the single-qubit transition matrix element, thus significantly reducing the time required for nuclear rotation. This mixing effect also renormalizes nuclear $|\mathrm{M_I}\rangle \rightarrow |\mathrm{M_I} \pm 1\rangle$ gaps, making the $|7/2\rangle \rightarrow |5/2\rangle$ transition distinguishable from all the others.

We finally note that, although in the idle state (with both electrons frozen in ↓) the qubits are practically decoupled, a weak residual interaction (mediated by electron virtual excitations) is still present. However, this is a tiny effect $\left[\sim \frac{A_1^2 J_x}{(g\mu_B B)^2}\right]$ that only influences the dynamics of the system in the long-time limit and can be reduced by increasing the static magnetic field.

Among the various examples of two-qubit entangling gates, we propose in this work the implementation of the controlled-phase ($C_\varphi$) gate. As mentioned in the main text, this gate adds a phase $\varphi$ only to the $|00\rangle$ component of the two-qubit wave-function, and it is thus represented (in the $\{|00\rangle, |01\rangle, |10\rangle, |11\rangle\}$ basis) by the matrix

$$U_{C_\varphi} = \begin{pmatrix} e^{-i\varphi} & 0 & 0 & 0 \\ 0 & 1 & 0 & 0 \\ 0 & 0 & 1 & 0 \\ 0 & 0 & 0 & 1 \end{pmatrix}.$$

Although it looks very simple, this transformation is able to generate maximally entangled states starting from factorized ones. The CZ gate is a particular $C_\varphi$ gate with $\varphi = \pi$.

As explained in the main text, the CZ is implemented by a full Rabi oscillation of the electron-spin component of the wave-function, conditioned by the state of the nuclei. This is obtained by a 2π-pulse resonant with the transition $|00\rangle|\mathrm{M_S} = -1\rangle \rightarrow |00\rangle|\mathrm{M_S} = 0\rangle$, that adds a $\pi$ phase to the $|00\rangle$ component.

Conversely, a semi-resonant pulse[3] can be exploited to implement a generic $C_\varphi$ gate. Indeed, if the 2π oscillating Gaussian pulse is detuned from the $|00\rangle|M_S = -1\rangle \rightarrow |00\rangle|M_S = 0\rangle$ transition of an amount δ, a phase $\varphi = \pi - \pi\frac{\delta}{\sqrt{4G^2+\delta^2}}$ is added. Here *G* represents the matrix element between the two involved states.

**Digital Quantum Simulation.** The simulation of quantum systems by a classical computer is intrinsically inefficient because the required number of bits grows exponentially with the system size. This makes many important problems in physics and chemistry intractable with standard computational approaches and resources. Such a limitation might be overcome by quantum simulators (QSs), whose dynamics can be controlled so as to mimic the evolution of the target system.[4] Quantum simulators can be broadly classified in two categories. In analog simulators the quantum hardware directly emulates another (target) quantum system, while in digital simulators the state of the target system is encoded in qubits and the time evolution of any target system can be discretized into a sequence of logical gates. While analog simulators are restricted to specific target problems, digital architectures are small, general purpose quantum computers, able to simulate broad classes of Hamiltonians.[5]

In this work, we propose our system for a proof-of-principle experiment of digital quantum simulation. Therefore, we now focus on how to decompose the time evolution induced by any target Hamiltonian into a sequence of elementary steps, controlled by the experimenter, i.e., a sequence of one- and two-qubit gates, as formalized by Lloyd.[6]

Most Hamiltonian of physical interest can be written as the sum of $L$ local (time-independent) terms, $\mathcal{H} = \sum_{k=1}^{L} \mathcal{H}_k$. Hence, the system dynamics can be approximated by a sequence of local unitary operators according to the Trotter-Suzuki formula ($\hbar = 1$):

$$U(t) = e^{-i\mathcal{H}t} \approx \left(e^{-i\mathcal{H}_1\tau} e^{-i\mathcal{H}_2\tau} \dots e^{-i\mathcal{H}_L\tau}\right)^n$$

where $\tau = t/n$ and the total digital error of this approximation can be made as small as desired by choosing $n$ sufficiently large.[6] Commuting terms in the Hamiltonian do not require any Trotter decomposition. In this way, the simulation reduces to the sequential implementation of local unitary operators, each one corresponding to a small time interval $t/n$. These can be implemented by a proper sequence of single- and two-qubit gates. The problem then reduces to finding a suitable mapping between the physical hardware (consisting of many qubits, described by means of Pauli algebra) and the target Hamiltonian $\mathcal{H}$.

The mapping of $s = 1/2$ models onto an array of qubits is straightforward. Let's consider here two kinds of significant local terms in the target Hamiltonian, namely one- ($\mathcal{H}_\alpha^{(1)}$) and two-body ($\mathcal{H}_{\alpha\beta}^{(2)}$) terms, with $\alpha = x, y, z$. The unitary time evolution corresponding to one-body terms $\mathcal{H}_\alpha^{(1)} = bs_\alpha$ is directly implemented by single-qubit rotations $R_\alpha(b\tau)$. Conversely, two-

body terms describe a generic spin-spin interaction of the form $\mathcal{H}^{(2)}_{\alpha\beta} = \lambda s_{1\alpha} s_{2\beta}$, for any choice of $\alpha, \beta = x, y, z$. The evolution operator, $e^{-i\mathcal{H}^{(2)}_{\alpha\beta}\tau}$ can be decomposed as:[7,8]

$$e^{-i\lambda s_{1\alpha} s_{2\beta}\tau} = \left[u_{1\alpha} \otimes u_{2\beta}\right] e^{-i\lambda s_{1z} s_{2z}\tau} \left[u_{1\alpha} \otimes u_{2\beta}\right]^{\dagger}$$

with $u_x = R_y\left(\frac{\pi}{2}\right)$, $u_y = R_x\left(\frac{3\pi}{2}\right)$, $u_z = I$.

The Ising evolution operator, $e^{-i\lambda s_{1z} s_{2z}\tau}$, can be obtained starting from the two-qubit $C_\varphi$ gate and exploiting the identity (apart from an overall phase)

$$e^{-i\lambda s_{1z} s_{2z}\tau} = U_{C_\varphi}\left[R_{1z}\left(-\frac{\varphi}{2}\right) \otimes R_{2z}\left(-\frac{\varphi}{2}\right)\right]$$

Here the $R_{iz}(\varphi)$ gates can be simultaneously implemented on both the involved qubits, by combining $R_x$ and $R_y$ rotations: $R_z(\varphi) = R_y^{\dagger}\left(\frac{\pi}{2}\right) R_x(\varphi) R_y\left(\frac{\pi}{2}\right)$.

This gate can also be directly implemented by exploiting the excited nuclear state $|M_I = 3/2\rangle$. Indeed, a 2π semi-resonant[3] rf pulse targeting the $|M_I = 5/2\rangle \rightarrow |M_I = 3/2\rangle$ transition can be used to add the desired phase to the $|1\rangle$ ($|M_I = 5/2\rangle$) component of the single-qubit wave-function (see above).

Besides the trivial case of spin-1/2 Hamiltonians, most models of physical interest can be re-written in terms of spin-1/2 operators. For instance, the simulation of Hamiltonians involving $S > 1/2$ spins can be performed by encoding the state of each spin *S* onto that of *2S* qubits. The example reported in the main text (the simulation of the quantum tunnelling of the magnetization for a *S* = 1 system) falls in this category. Indeed, we have re-written the total spin *S* as $s_1 + s_2$ and then mapped the quadratic terms in the target Hamiltonian $S_\alpha^2$ into $2s_{1\alpha} s_{2\alpha}$:

$$S_\alpha = s_{1\alpha} + s_{2\alpha}$$

$$S_\alpha^2 = (s_{1\alpha} + s_{2\alpha})^2 = 2s_{1\alpha} s_{2\alpha} + \text{const.}$$

A sketch representing the mapping of the target S=1 system into the hardware Hamiltonian is reported in Figure S12. The nuclear qubits (bottom) are the physical hardware, consisting of $s_i = 1/2$ qubits (red arrows). These are used to encode the target Hamiltonian, consisting of a

giant $S = 1$ (blue arrow). The corresponding time evolution is then simulated as outlined above. In particular

$$e^{-i\varphi s_{1x}s_{2x}} = R_y\left(\frac{\pi}{2}\right) e^{-i\varphi s_{1z}s_{2z}} R_y^{\dagger}\left(\frac{\pi}{2}\right)$$

with

$$e^{-i\varphi s_{1z}s_{2z}} = U_{C_\varphi} R_z\left(-\frac{\varphi}{2}\right)$$

and $R_z\left(-\frac{\varphi}{2}\right) = R_y^{\dagger}\left(\frac{\pi}{2}\right) R_x\left(-\frac{\varphi}{2}\right) R_y\left(\frac{\pi}{2}\right)$. Here $R_\alpha(\varphi)$ are simultaneous rotations on both qubits. By combining these decompositions, we obtain the pulse sequence reported in Fig. 5, where some gates cancel each other out. Indeed, by collecting all the unitary gates together we find:

$$e^{-i\varphi s_{1x}s_{2x}} = R_y\left(\frac{\pi}{2}\right) U_{C_\varphi} R_y^{\dagger}\left(\frac{\pi}{2}\right) R_x\left(-\frac{\varphi}{2}\right) R_y\left(\frac{\pi}{2}\right) R_y^{\dagger}\left(\frac{\pi}{2}\right) = R_y\left(\frac{\pi}{2}\right) U_{C_\varphi} R_y^{\dagger}\left(\frac{\pi}{2}\right) R_x\left(-\frac{\varphi}{2}\right).$$

We finally note that, due to the symmetric role of the two qubits, the system dynamics is restricted to the $S = 1$ subspace, corresponding to the target Hamiltonian. For instance, if the system is initialized in 00 (as in the simulation reported in the main text), gates corresponding to the evolution $e^{-iD\sigma_{1z}\sigma_{2z}t/2\hbar}$ do not affect the system dynamics. Hence, the giant spin oscillates between opposite sides of the anisotropy barrier ($M = \pm 1$) as a result of the rhombic term in the target Hamiltonian.

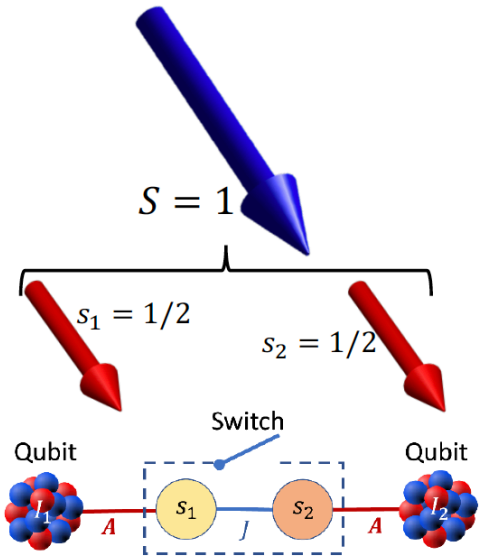


**Figure S12**. Mapping between the physical hardware (a pair nuclear spins with a switchable interaction), the $s_i = 1/2$ qubits and the target $S = 1$.

**Initialization.** At experimentally achievable temperatures all the (nuclear) computational basis states are nearly equally populated, while a sufficiently large magnetic field ensures electron polarization. Pumping techniques[9,10,11] exploiting a proper combination of microwave (mw) and radio-frequency (rf) pulses[11] could be used to transfer polarization from electronic to nuclear spins, thus initializing the system in a practically pure state. The procedure is exemplified in Ref. [11] for a single NV center: let $|m_I m_s\rangle$ be the initial state of the system, with equal population on all $m_I$ states (fully depolarized nuclear spin) and only the electronic ground $m_s = g_s$ state populated. The aim is to transfer population to the ground nuclear state $g_I$. Mw π pulses are used to induce the transitions $|m_I g_s\rangle \rightarrow |m_I e_s\rangle$ for all $m_I \neq g_I$, thus exciting the electronic spins to $e_s$. Then, rf π pulses are applied to transfer population between the excited electron states, from $|m_I e_s\rangle$ to $|g_I e_s\rangle$. These transitions are spectroscopically resolved from those within the $m_s = g_s$ manifold, thanks to the hyperfine interaction. Finally, electronic spins are re-polarized by a laser pulse.

A similar procedure could be envisaged here, by letting the electron spin relax to its ground state (from $|g_I e_s\rangle$ to $|g_I g_s\rangle$), thus increasing the nuclear polarization. This works under the safe assumption that nuclear spin relaxation times (and also cross relaxation times) are much longer than the electron spin relaxation times.

Alternatively, only the first step (excitation of unwanted nuclear states by mw π pulses) is sufficient to freeze populations not corresponding to the right initial nuclear state.

**Spectral resolution required for controlled-Z gates.** As explained in the main text, the energy required to excite the electron spins is renormalized by the effective magnetic field produced by the hyperfine coupling with the nuclear spins. This allows us to implement an entangling controlled-Z (CZ) two qubit gate.

However, in the present regime of parameters (with $A_z > J_x$), the spectral resolution required to implement a CZ gate results from the combined effect of both hyperfine and exchange interactions. Indeed, the energy difference between the $|00\rangle|M_S = -1\rangle \rightarrow |00\rangle|M_S = 0\rangle$ and the closest unwanted transition is $\Delta = \frac{A_z}{2} + \frac{J_x+J_y}{4} - \frac{1}{2}\sqrt{A_z^2 + \frac{(J_x+J_y)^2}{4}}$ (z being the direction of the static field). Here transverse components of A have been neglected for simplicity, since $A_{x,y} \ll g\mu_B B$. This expression for the closest unwanted excitation motivated the choice of z as the direction of the external field. Indeed, putting the field in this direction maximizes Δ. Notice that in the large-*J* limit the Δ reduces to $\frac{A_z}{2}$, while if $A_z \gg J_{x,y}$ it only depends on the transverse component of the exchange interaction.

## SUPPLEMENTARY REFERENCES


1. Breuer, H.-P.; Petruccione, F., *The theory of Open Quantum Systems* (Oxford University Press, 2002).

2. M. A. Nielsen, I. L. Chuang, *Quantum Computation and Quantum Information* (Cambridge University Press, Cambridge, England, 2000).

3. M. Mariantoni, H. Wang, T. Yamamoto, M. Neeley, R. C. Bialczak, Y. Chen, M. Lenander, E. Lucero, A. D. O'Connell, D. Sank, M. Weides, J. Wenner, Y. Yin, J. Zhao, A. N. Korotkov, A. N. Cleland, J. M. Martinis, *Science*, 2011, **334**, 61.

4. R. P. Feynman, *Int. J. Theor. Phys.*, 1982, **21**, 467.

5. I. M. Georgescu, S. Ashab, F. Nori, *Rev. Mod. Phys.*, 2014, **86**, 153.

6. S. Lloyd, *Science*, 1996, **273**, 1073.

7. P. Santini, S. Carretta, F. Troiani, G. Amoretti, *Phys. Rev. Lett.*, 2011, **107**, 230502.

8. A. Chiesa, P. Santini, D. Gerace, J. Raftery, A. A. Houck, S. Carretta, *Sci. Rep.*, 2015, **5**, 16036.

9. A. S. Verhulst, O. Liivak, M. H. Sherwood, H.-M. Vieth, I. L. Chuang, *Appl. Phys. Lett.*, 2001, **79**, 2480–2482.

10. K. Sato, S. Nakazawa, R. Rahimi, T. Ise, S. Nishida, T. Yoshino, N. Mori, K. Toyota, D. Shiomi, Y. Yakiyama, Y. Morita, M. Kitagawa, K. Nakasuji, M. Nakahara, H. Hara, P. Carl, P. Hofer, T. Takui, *J. Mater. Chem.*, 2009, **19**, 3739-3754.

11. T. Chakraborty, J. Zhang, D. Suter, *New J. Phys.*, 2017, **19**, 073030.

12. M. Mrózek, J. Mlynarczyk, D. S. Rudnicki, W. Gawlik, *Appl. Phys. Lett.*, 2015, **107**, 013505.